ACS Energy LETTERS

http://pubs.acs.org/journal/aelccp

LETTER

Influence of Electrode Interfaces on the Stability of Perovskite Solar Cells: Reduced Degradation Using MoO_x/Al for Hole Collection

Erin M. Sanehira,[†,‡] Bertrand J. Tremolet de Villers,[†] Philip Schulz,[†] Matthew O. Reese,[†] Suzanne Ferrere,[†] Kai Zhu,[†] Lih Y. Lin,[‡] Joseph J. Berry,[†] and Joseph M. Luther*[,†]

[†]National Renewable Energy Laboratory, Golden, Colorado 80401, United States

[‡]Department of Electrical Engineering, University of Washington, Seattle, Washington 98195, United States

Supporting Information

ABSTRACT: We investigated and characterized the stability of the power output from methylammonium lead iodide perovskite photovoltaic devices produced with various hole-collecting anode configurations consisting of Au, Ag, MoO_x/Au, MoO_x/Ag, and MoO_x/Al. The unencapsulated devices were operated under constant illumination and constant load conditions in laboratory ambient with periodic current−voltage testing. Although the initial efficiencies of devices were comparable across these configurations, the stability of these devices varied significantly due to subtle differences in the electrode structure. Specifically, we found that devices with MoO_x/Al electrodes are more stable than devices with more conventional, and more costly, Au and Ag electrodes. We demonstrate that a thin MoO_x layer inhibits decomposition of the perovskite films under illumination in ambient laboratory conditions and greater improvements in device stability are achieved specifically with MoO_x/Al electrodes. We investigated the role of the MoO_x interlayer in the MoO_x/Al electrodes by exploring the effect of relative humidity and the MoO_x interlayer thickness on the perovskite solar cell stability.

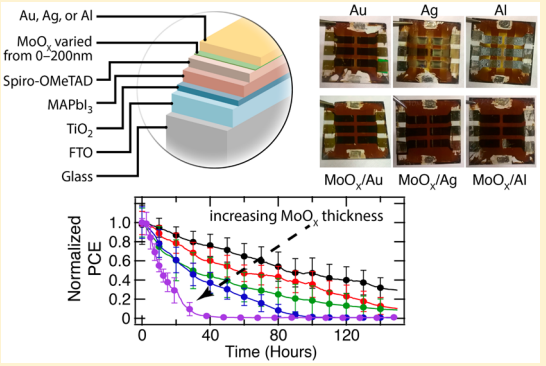

Organic−inorganic metal halide perovskite semiconductors have garnered significant interest from the research community with solar cell power conversion efficiencies (PCEs) above 22% recently.[1] Halide perovskites, such as $CH_3NH_3PbI_3$ ($MAPbI_3$), have low crystal formation energies[2] and are amenable to solution processing while also possessing favorable optoelectronic properties such as high optical absorption,[3] high ambipolar mobilities,[4] and unique tolerance to structural defects.[5,6] Although a plethora of work has been and continues to be conducted on film deposition techniques,[7−10] surface passivation,[11−13] and device architectures[14,15] to improve PCEs, device stability still remains a primary concern.[16,17]

Recently, stability studies have been conducted on $MAPbI_3$ films and devices and have provided insight on the role of light, heat, and ambient environmental conditions.[15,18−24] Several reviews regarding stability have recently been published.[16,25,26] Due to the many factors that affect device stability (e.g., humidity, illumination, temperature, etc.), comparing stability results can be intractable without standardized testing protocols. Although the perovskite research community has not established standardized stability testing procedures, leading organic photovoltaic researchers outlined specific protocols at the third International Summit on OPV Stability (ISOS).[27] Using these laboratory weathering protocols, specifically ISOS-L-1, we characterized the degradation of perovskite solar cells under constant operating conditions under illumination and exposed to laboratory ambient conditions. All of the solar cells characterized in this study were unencapsulated to simulate the complex interaction of illumination, environmental agents, and various components in the device architecture that are relevant to real world applications. Although encapsulated perovskite solar cells have yielded relatively high lifetimes of hundreds of hours,[7,28] encapsulant materials inevitably allow some moisture ingress over time.[29] Hardening a device structure to ambient

Received: March 10, 2016
Accepted: April 14, 2016

DOI: 10.1021/acsenergylett.6b00013
ACS Energy Lett. 2016, 1, 38−45

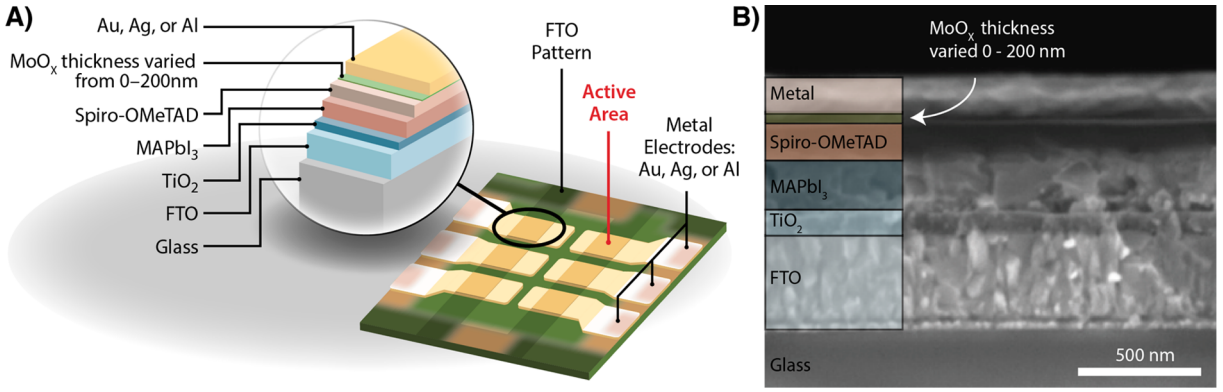

Figure 1. (A) Schematic representation of the layer structure in cross section and top-down views of a completed photovoltaic device. The active area of a solar cell is defined by the overlap of the metal electrode and patterned FTO strip, denoted as the darker gold region on the metal electrodes. During measurement, a metal aperture mask is placed over the glass substrate with precisely positioned holes to ensure that illumination only occurs on the active area. Each substrate has six individual devices. (B) Scanning electron microscopy cross-sectional image of a perovskite solar cell with individual layers labeled.

environmental conditions is preferable to relying on packaging, which can be costly and may fail, for protection.

Some approaches to device hardening include employing alternative perovskite active layer chemistries,[30,21,31,32] incorporating buffer layers,[18,33,34] or introducing more robust or hydrophobic hole-transporting layers (HTLs) and electrodes.[35−38] Previous reports have mentioned stability issues with Ag[28,39] or Al[40] electrodes in perovskite devices, which has led most researchers to rely on expensive Au electrodes. Kato et al.,[41] for example, have shown that $MAPbI_3$ iodizes Ag electrodes and concluded that further work in reducing this iodization of the Ag electrode is necessary. To address electrode corrosion, Guerrero et al.[43] demonstrated greater electrode stability with a Cr_2O_3/Cr electrode in inverted, planar perovskite solar cells. Similarly, Back et al.[42] implemented a chemical inhibition layer to prevent corrosion of Ag and Al electrodes. It is unclear, however, how the stability of these modified electrodes compares with that of relatively inert Au electrodes and whether these solutions are compatible with more conventional perovskite solar cell device architectures.

Although Au and Ag are most commonly used for the metal electrodes in organic−inorganic perovskite solar cells, Zhao et al. previously reported that a thin molybdenum oxide (MoO_x) layer enables the use of Al as a cost-effective electrode alternative.[44] This type of contact uses an oxygen-deficient molybdenum trioxide layer, which has a high work function that enables efficient hole extraction.[45] Furthermore, MoO_x can also be paired with conventional electrode metals such as Ag[44,46] and Au[47] in perovskite solar cells. MoO_x interlayers have been previously demonstrated to improve the performance and stability of organic light-emitting diodes,[48,49] organic photovoltaics,[50−52] and quantum dot solar cells;[53,54] however, the effect of a MoO_x back electrode on a perovskite solar cell's stability has not been explored.

Here, we study the effects of using various hole-collecting anode configurations on the initial $MAPbI_3$ solar cell efficiency and the device stability. Specifically, we examine the effect of adding a MoO_x hole-extraction layer to commonly used metals such as Au, Ag, and Al, as shown in Figure 1. First, we find that adding a thin (15 nm) MoO_x layer on $MAPbI_3$/spiro-OMeTAD films provides conformal coverage and reduces decomposition of the $MAPbI_3$ films under illumination in ambient conditions. Next, we fabricated devices with MoO_x/Al electrodes and characterized the stability in various humidity conditions. To determine if the MoO_x was serving as an encapsulation layer, we varied the thickness of the MoO_x layer and found that although all devices possess similar initial efficiency, the devices with thinner MoO_x are more stable over time. These results indicate that the MoO_x is not improving the device by reducing the amount of moisture introduced to the device. Instead, the device stability is likely enhanced by specific details at the MoO_x/Al interface, which do not affect the initial device efficiency. We then observed a greater resistance to degradation for devices employing a MoO_x/Al electrode as compared to devices with more conventional Au or Ag electrodes. Furthermore, the device durability is not only dependent on the use of a MoO_x hole-extraction layer but more specifically dependent on the MoO_x/metal combination with MoO_x/Al electrodes yielding the highest stability. We emphasize that *all stability studies were conducted by operating devices with different electrode configurations under constant illumination and constant resistive load in laboratory ambient conditions*. By monitoring the devices during constant operation, we observe significant differences in the degradation behavior of devices employing different back electrode configurations.

Earlier work by Ono et al.[37] and Yang et al.[19] suggest that the HTLs, such as spiro-OMeTAD, can mitigate decomposition of an underlying $MAPbI_3$ film; however, poor continuity in the HTL allows the ingress of moisture and the egress of volatile decomposition products. Thus, we hypothesized that evaporating a thin layer of MoO_x could effectively fill pinholes in the spiro-OMeTAD film and reduce moisture ingress to the $MAPbI_3$ film. We performed XPS studies on $MAPbI_3$/spiro-OMeTAD films with and without a MoO_x layer on top to compare the coverage and conformity of the spiro-OMeTAD and MoO_x films on the $MAPbI_3$ layer. In the XPS spectra shown in Figure 2A,B, we see the presence of the I 3d and Pb 4f core levels, respectively, on the surface of $MAPbI_3$/spiro-OMeTAD films without MoO_x, in contrast to the absence of these I 3d and Pb 4f signals on the surface of devices with a MoO_x layer on top. The presence of Pb and I signals is consistent with reports in the literature that indicate pinhole formation in the ∼100 nm thick spiro-OMeTAD layer.[37] It has been suggested that these pinholes provide a path for moisture and oxygen ingress to degrade the absorber.[37] By filling in

DOI: 10.1021/acsenergylett.6b00013
ACS Energy Lett. 2016, 1, 38−45

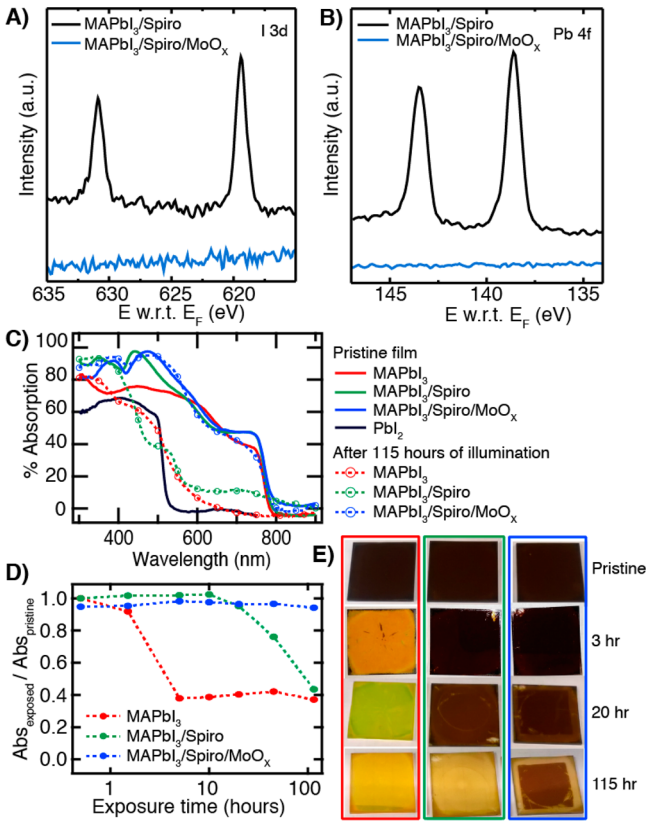

Figure 2. XPS core level spectra of (A) I 3d and (B) Pb 4f regions of $MAPbI_3$/spiro-OMeTAD films on TiO_2 with (in blue) and without (in black) a MoO_x layer. The emergence of features in the glass/TiO_2/$MAPbI_3$/spiro-OMeTAD case is consistent with pinhole formation in the spiro-OMeTAD layer. The 15 nm thick MoO_x layer on top obscures any evidence of iodine or lead, which is consistent with the concept of sealing of these pinholes. (C) Absorption spectra of bare $MAPbI_3$ (red), $MAPbI_3$/spiro-OMeTAD (green), and $MAPbI_3$/spiro-OMeTAD/MoO_x (blue) films on glass/TiO_2 before and after 115 h of illumination. Degradation was induced by constant illumination from a tungsten−halogen light source in ambient conditions. The absorption spectrum of PbI_2 (black) is also provided. (D) The ratio of absorption by the exposed film relative to the pristine film over light exposure time. The absorption was quantified by integrating the absorption spectrum of the film with the AM1.5 solar spectrum. (E) Optical images of the films with increasing light exposure show the decomposition of the $MAPbI_3$ film from brown to yellow with increasing light exposure. The films pictured here were deposited on 1 in. × 1 in. glass slides. Because the MoO_x layer was deposited through a shadow mask, the edges of the $MAPbI_3$/spiro-OMeTAD/MoO_x sample were bleached where the MoO_x is absent, but the protected center remained optically dark.

pinholes in the spiro-OMeTAD layer, it is likely that the MoO_x interlayer can suppress degradation of the $MAPbI_3$ layer.

To determine the effect of the MoO_x interlayer on the degradation of $MAPbI_3$ films, we monitored the absorptance of $MAPbI_3$ films with prolonged light exposure in ambient laboratory conditions. We compared the absorption of (i) $MAPbI_3$, (ii) $MAPbI_3$/spiro-OMeTAD, and (iii) $MAPbI_3$/spiro-OMeTAD/MoO_x film stacks on glass/TiO_2 substrates. The films were illuminated by an Eiko Solux tungsten−halogen light source set to a light intensity equivalent to 1 sun flux in laboratory ambient conditions. After 115 h of illumination, the absorption spectra of the $MAPbI_3$ and $MAPbI_3$/spiro-OMeTAD films without MoO_x exhibited significant absorption losses in the spectral region between 500 and 800 nm, which indicates degradation of the $MAPbI_3$ film. The degraded $MAPbI_3$ and $MAPbI_3$/spiro-OMeTAD absorption spectra resemble the absorption spectrum of PbI_2, which has an absorption onset at about 520 nm. In contrast, most of the absorption of the $MAPbI_3$/spiro-OMeTAD/MoO_x film was retained except for slight reduction in the absorption throughout the 650−800 nm wavelength regime. This reduction in absorption was significantly less than that of the $MAPbI_3$ and $MAPbI_3$/spiro-OMeTAD films in the same wavelength region and occurred after a much greater duration of light exposure (Figure S1), indicating an enhanced stability from the MoO_x layer. Furthermore, we did not observe any absorption losses in films stored under dark conditions for 115 h (Figure S2), which indicates that illumination played a critical role in the degradation of these $MAPbI_3$ films.

To quantify the loss in the absorption over time, the spectral absorptance was integrated with the AM1.5G solar spectrum to calculate the number of solar photons that would be absorbed by each film after light exposure. We then normalized this number of solar photons absorbed by the light-exposed film relative to the initial, pristine film, which is provided in Figure 2D. This ratio of absorption by the light-exposed film relative to the pristine film declined rapidly after a mere 1.5 h of light exposure and then plateaued at roughly 40% for the $MAPbI_3$ film. Adding a spiro-OMeTAD film on the $MAPbI_3$ film retarded this reduction in absorptance until 10 h of light exposure, after which the absorptance deteriorated to the same 40% of initial absorptance as the $MAPbI_3$ film. More importantly, when a thin (15 nm) MoO_x layer was deposited on the $MAPbI_3$/spiro-OMeTAD stack, 94% of the initial absorptance was retained after 115 h of illumination. These results indicate that the MoO_x mitigates photoinduced decomposition of the $MAPbI_3$ film.

We can also see these trends in the photographs of the films in Figure 2E. The initially dark brown $MAPbI_3$ film turned yellow after 3 h of light exposure and remained yellow with continued light exposure, which corresponds with the plateau in the absorption loss in Figure 2D. The $MAPbI_3$/spiro-OMeTAD films also turned yellow after 115 h, whereas the $MAPbI_3$/spiro-OMeTAD/MoO_x film only lightened slightly after 115 h of illumination, which corresponds with the slight absorption loss in the 650−800 nm regime in Figure 2C. The observed transformation of the dark brown $MAPbI_3$ film to the resultant yellow film is consistent with previous reports of $MAPbI_3$ degradation to PbI_2.[16,22,30] X-ray diffraction (XRD) patterns of the samples after 115 h of illumination (Figure S3) is consistent with the decomposition of $MAPbI_3$ to PbI_2. The $MAPbI_3$/spiro-OMeTAD stack and $MAPbI_3$ film did not reveal any clear diffraction peaks after degradation and appeared significantly more disordered. We suggest that this is due to further decomposition of the PbI_2 under continued exposure to illumination and ambient oxygen and moisture.

To support the hypothesis of moisture and/or oxygen ingress being deleterious to device performance and determine whether a thin MoO_x layer can serve as an effective moisture barrier, we examined three sets of devices with MoO_x/Al electrodes degraded with different ambient humidity due to seasonal variations in our lab. As expected, we found increasing levels of relative humidity (RH) to accelerate degradation rates. Several devices with the same device configuration were fabricated and tested in low, medium, and high RH conditions

DOI: 10.1021/acsenergylett.6b00013
ACS Energy Lett. 2016, 1, 38−45

with humidity ranges of 16 ± 4, 33 ± 9, and 51.5 ± 1.5, respectively. The normalized efficiency of representative devices and the recorded humidity data are provided in Figure 3 (see

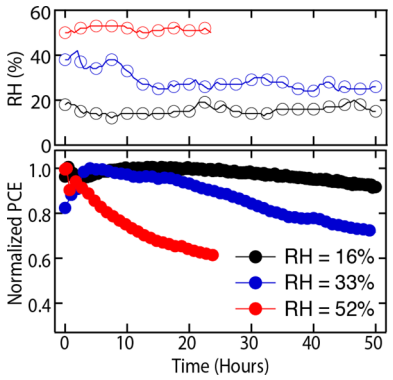

Figure 3. Normalized PCE of similarly fabricated cells measured in three different RH conditions. All of the devices had the same electrode configuration of 15 nm of MoO_x/200 nm of Al.

the Supporting Information for details regarding device measurement). The device tested in high RH had degraded to roughly 61% of the initial efficiency after 24 h of operation, whereas the devices in the medium and low RH conditions were still at 90 and 99%, respectively, of the initial efficiency after the first 24 h of operation. After 50 h of operation, the devices in medium and low RH conditions had maintained roughly 71 and 91%, respectively, of the initial device efficiency, which further corroborates the moisture sensitivity of the $MAPbI_3$ films and devices previously reported.[19,39] Although a 15 nm layer of MoO_x may be retarding the level of moisture/oxygen ingress, there is still a clear sensitivity to humidity.

To explore the possibility of improving the barrier properties of the MoO_x interlayer, we varied the MoO_x interlayer thickness and fabricated devices with MoO_x thicknesses of 8, 15, 50, 100, and 200 nm. The initial measurement of the devices yielded average device efficiencies ranging from 9.2 to 9.8%, as seen in Figure 4B. Among the devices selected for stability testing, the initial device performance did not have a strong thickness dependence, which is unlike the study by Zhao et al. that found a decrease in PCE with MoO_x thicknesses exceeding 10 nm.[44] We did, however, observe a lower yield in measurable devices for the 8 nm MoO_x case (Figure S5), indicating that 8 nm may not provide complete coverage.

After the initial measurement, the devices with varying MoO_x interlayer thicknesses were operated in laboratory ambient for 150 h. As the stability testing setup used a sulfur plasma light source, current density−voltage (J−V) characteristics under an AM1.5G solar simulator were acquired before and after the laboratory weathering. Despite having comparable initial efficiencies across the varying MoO_x thicknesses, devices with thicker MoO_x interlayers had lower PCEs after constant operation for 150 h in ambient, as seen by the open squares in Figure 4B. In this case, the inverse correlation between MoO_x thickness and device lifetime is more apparent from the measurements taken in ambient during constant operation, as seen in Figure 4C. This is due to the rapid decline in device performance in the first 25 h for the 50 nm MoO_x devices, which cannot be observed by the single postdegradation measurement in Figure 4B.

From visual inspection of the degraded devices, we observe corrosion under the metal electrodes for the thinner 8 and 15 nm MoO_x devices but not for the devices with thicker MoO_x interlayers. Thus, the thicker MoO_x interlayers help prevent corrosion under the Al electrodes, but this corrosion is not the primary cause of device failure as it occurs outside of the active device area. Instead, we see faster degradation in device performance with the thicker MoO_x layers but without many visual indicators for this decrease in stability. The degradation in performance also corresponds with a rapid increase in series resistance during the continuous operation of the devices with

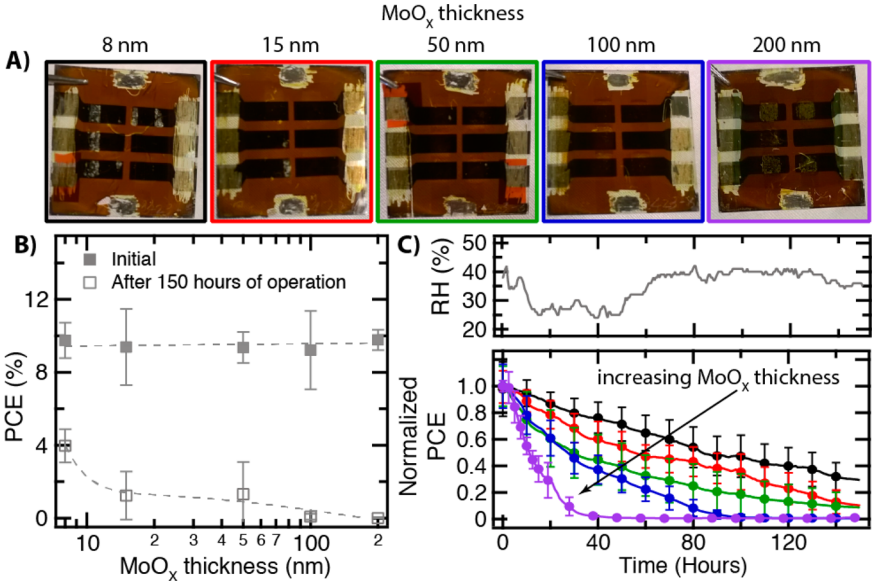

Figure 4. (A) Optical images of the devices with MoO_x/Al electrodes with varying thicknesses of MoO_x after 150 h of constant operation. The devices pictured here were fabricated on 1 in. × 1 in. glass substrates. (B) The efficiency of devices before (closed squares) and after 150 h of constant operation (open squares) measured in a N_2-filled glovebox. (C) The RH and normalized efficiency of devices measured during the 150 h of operation. The normalized average efficiency of devices with MoO_x thicknesses of 8, 15, 50, 100, and 200 nm are shown in black, red, green, blue, and purple, respectively. Error bars shown represent one standard deviation of the measured cells.

DOI: 10.1021/acsenergylett.6b00013
ACS Energy Lett. 2016, 1, 38−45

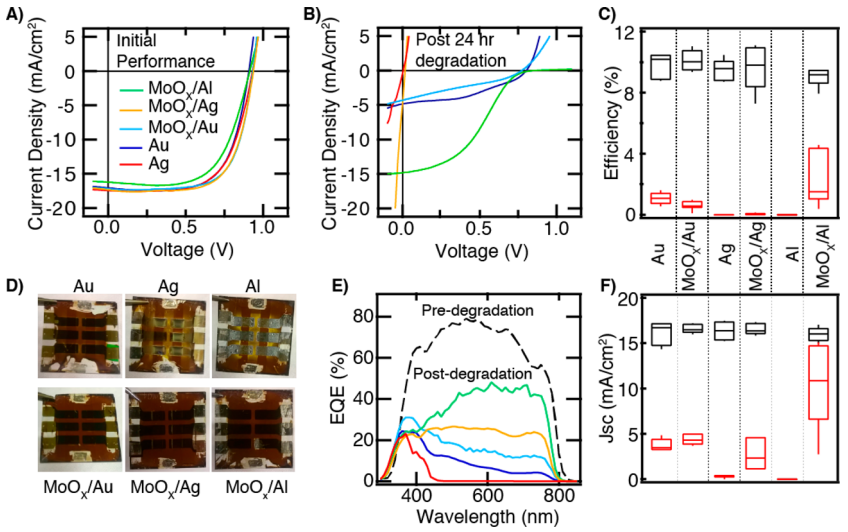

Figure 5. Current density−voltage characteristics of representative devices with Au (dark blue), Ag (red), MoO_x/Au (light blue), MoO_x/Ag (orange), or MoO_x/Al (light green) electrodes (A) before and (B) after 24 h of constant operation in ambient. The MoO_x interlayers had a thickness of 15 nm. (C) Box plots of the efficiency before (black) and after (red) degradation. (D) Optical images taken from the glass side of the device show visual signs of $MAPbI_3$ decomposition for devices without the MoO_x interlayer. The devices pictured here were fabricated on 1 in. × 1 in. glass substrates. (E) External quantum efficiency of the devices after 24 h of constant operation. The EQE spectra of a typical as-prepared device is also shown in black. (F) Box plots of the short-circuit current density show that the relative postdegradation short-circuit current corresponds with the area under the EQE spectra.

thicker MoO_x interlayers (Figure S6). This inverse correlation between the MoO_x thickness and the device lifetime is consistent with an interfacial effect between the MoO_x and Al or spiro-OMeTAD layers, a bulk compositional change to the MoO_x, or some combination of these rather than the MoO_x interlayer acting as a moisture/oxygen barrier. More specifically, mechanisms for this reduction in durability with increasing MoO_x interlayer thickness may include the following: First, the increased MoO_x interlayer thickness may lead to an increase in delamination due to an increase in strain. Second, a larger MoO_x interlayer may correspond to greater, electrically driven Al_2O_3 formation at the MoO_x/Al interface. Third, the MoO_x layer may undergo compositional changes either with the relative oxygen content or through interaction with outward diffused Pb and/or I. Changes to the oxidation state have been shown to vary the work function,[55] resistivity,[56] and gap state density[57] of MoO_3. Each of these potential mechanisms is consistent with the reduced charge extraction observed with time. Currently, further studies are required to determine the root cause of the inverse MoO_x thickness dependence on the device stability.

We compared devices where the back electrode was Au, Ag, or Al either with or without a MoO_x interlayer, thus producing six electrode combinations. In the devices containing MoO_x, a thin layer of 15 nm was introduced between the spiro-OMeTAD HTL and the back metal electrode, as shown in Figure 1. With the exception of the Al-only electrode, the initial performance of devices with these different electrode configurations were comparable, as seen in the $J-V$ characteristics in Figure 5A. The median PCE of the devices varied from 9.2 to 10.2%, with the lowest-performing devices having a MoO_x/Al electrode and the highest-performing devices having a Au electrode, as seen in Figure 5C (black box plots). Devices with Al-only electrodes resulted in efficiencies of <0.1%, which is consistent with previous work by Zhao et al.[44] In the case of Au and Ag, the MoO_x interlayer was not necessary to yield working devices and did not affect the initial performance significantly.

After 24 h of constant operation in laboratory ambient, the MoO_x/Al electrodes, not commonly used in perovskite solar cells, retained the highest PCE of initially comparable devices. Devices with Au and MoO_x/Au electrodes showed the second- and third-highest PCEs after 24 h, respectively. The RH of the laboratory averaged 51.5 ± 1.5% during this test period. Similar to the previous stability tests, $J-V$ measurements were acquired with an AM1.5G solar simulator before and after weathering. The $J-V$ curves of champion cells are shown in Figure 5B, and the efficiencies are shown in the red box plots in Figure 5C. In the case of MoO_x/Al electrodes, the enhanced stability can be attributed to greater preservation of the short-circuit current density (J_{sc}), whereas a more stable open-circuit voltage (V_{oc}) and fill factor (FF) are responsible for the relatively high performance of the Au devices. Although Ag is often used in $MAPbI_3$ solar cells, we note that neither the Ag nor the MoO_x/Ag devices survived the degradation run, with average PCEs below 0.1% after 24 h of constant operation. This result is consistent with other reports of poor stability and corrosion of Ag electrodes in perovskite devices.[39,41]

A comparison of the J_{sc} of the degraded devices in Figure 5F reveals that devices with the MoO_x interlayer had higher J_{sc} than devices without MoO_x for all three metals used in this study. External quantum efficiency (EQE) spectra in Figure 5E provides greater insight on the relative improvements observed by adding a MoO_x interlayer. First, we see that the devices with Au or Ag electrodes without MoO_x have significant EQE losses in the longer-wavelength regime. This is similar to the absorption spectrum of the degraded $MAPbI_3$ films shown in Figure 2C and is consistent with a reduction in charge generation due to decomposition of the perovskite active layer. In the case of Au, adding a MoO_x interlayer resulted in a slight improvement in the EQE relative to the Au-only devices, but overall, the MoO_x/Au devices still suffered a significant loss in the longer-wavelength regime relative to the predegraded

DOI: 10.1021/acsenergylett.6b00013
ACS Energy Lett. 2016, 1, 38−45

device. Comparing the Ag and MoO_x/Ag devices, we see that the additional MoO_x interlayer preserves significantly more of the EQE in the longer-wavelength regime. The EQE of the degraded MoO_x/Al device shows the greatest preservation in shape relative to a predegraded device and the highest EQE overall. Thus, we see that the enhanced stability in the MoO_x-containing devices is affected by the choice of metal electrode. Although the choice of metal electrode did not affect the initial performance, we see that electrode choice has a significant effect on device degradation.

To gain insight into the increased stability of MoO_x/Al devices as compared to MoO_x/Au and MoO_x/Ag devices, we conducted XPS studies on thin, 5 nm metal films (Au, Ag, and Al) on bare ITO and on ITO/MoO_x substrates. In these studies, we can see that Au and Ag do not react with the MoO_x surface in Figure S8. The Al, however, does react with the underlying MoO_x film, which results in the formation of metallic Mo and MoO_2, as seen from the appearance of Mo^0 and Mo^{4+} components, respectively. We speculate that due to the relative formation enthalpy of Al_2O_3 ($\Delta_f H$ = −1669.8 kJ/mol) compared to that of MoO_3 ($\Delta_f H$ = −745.17 kJ/mol),[58] we may be forming Al_2O_3, or other nonstoichiometric aluminum oxides, at the MoO_x/Al interface. Previous studies have suggested that Al_2O_3 interlayers improve device stability by serving as a physical barrier to moisture.[18,34] While this remains a possibility, it seems peculiar that a thin alumina layer would impart so much better of a barrier than the thick metal layers. It also does not fully explain the observed differences in the EQE spectra of Figure 5E.

Visual inspection of the degraded devices reveals some further insight. As seen in Figure 5D, photographs of the devices without a MoO_x interlayer exhibit photobleaching in areas below or near the metal electrode after 24 h of operation in ambient. This photobleaching of the dark brown $MAPbI_3$ layer yielded a yellow film similar to the degraded $MAPbI_3$ films seen in Figure 2E and indicates decomposition of the $MAPbI_3$ layer. Using Ag or Al without MoO_x results in the most photobleaching, whereas Au electrodes without MoO_x result in some, but significantly less, photobleaching. This is consistent with Au, a noble metal, being significantly less reactive with the perovskite active layer than both Al and Ag. It also suggests that the MoO_x interlayer mitigates this reaction.

Visual indications of corrosion of the metal electrode are present in both the Al and MoO_x/Al cases. More specifically, we observe areas of transparency beneath the Al and MoO_x/Al electrodes (denoted in Figure S9). This occurs next to the FTO pad but not in the device's active area. This indicates that a different degradation mechanism may occur when an Al contact is used. The presence of the transparent areas beneath the Al electrodes, instead of either brown (indicating $MAPbI_3$) or yellow (indicating PbI_2) areas, suggests that the formation of PbI_2 is either inhibited or decomposed further due to the presence of Al. In the case of the MoO_x/Al devices, the active areas were not affected appreciably and were still operable.

Taking these different pieces together, we propose a potential mechanism. First we review the relevant observations. Devices with Au electrodes appear to degrade in a manner similar to the noncontacted samples in Figure 2E. Introducing a thin MoO_x layer to a device with Au electrodes has only a mild effect in reducing the degradation of the perovskite active layer. However, the presence of a reactive metal such as Ag or Al without a protective interlayer accelerates the active layer decomposition. Inserting a MoO_x interlayer significantly slows the active layer decomposition when Ag or Al is used, even relative to the Au case (Figure 5E). Increasing the thickness of the MoO_x layer accelerates degradation, suggesting that MoO_x is not primarily serving as a moisture barrier layer. Depositing Al or Ag on a thin oxide layer can lead to an interfacial oxide that would not form when deposited on spiro-OMeTAD. Al in particular not only has an oxide with a high tendency to form but is also a strongly passivating oxide as a result of its Pilling–Bedworth ratio (ratio of volume of elemental cells of the oxide to metal). Devices with MoO_x/Au contacts compared to Au-only experience little alteration in the EQE spectrum as a result of degradation. In contrast, Ag- and Al-based devices see a dramatic change in their spectral response compared to their counterparts with MoO_x, which suggests that the MoO_x benefit is related to the formation of a protective oxide. The fact that increased MoO_x thickness is detrimental to stability further supports that the role of the MoO_x is connected to interfacial stability. Changing series resistance of the MoO_x thickness series suggests that MoO_x may have its composition evolve with time. Very thin layers may serve to pin the work function at the spiro-OMeTAD interface while nucleating a stable oxide at the metal interface. The self-passivating nature of aluminum oxide explains the increased stability of MoO_x/Al over MoO_x/Ag. The introduction of Al (or Ag) oxide then leads to the slowing of iodization of the back contact. This work directly addresses the previously identified need to minimize iodization in Ag back contacts while preserving initial efficiency and without requiring a significantly altered device architecture.

In conclusion, we demonstrated that electrode selection for $MAPbI_3$ devices has a profound effect on the device stability despite having comparable initial efficiencies. Specifically, MoO_x/Al electrodes yielded the most stable solar cells. Furthermore, while we find that MoO_x thickness has little impact on the initial efficiency, thinner MoO_x interlayers yield more durable devices. These results are consistent with enhanced stability due to an interfacial effect with the MoO_x. The absorption spectra and XRD patterns of illuminated $MAPbI_3$ films indicate that a thin MoO_x layer prevents photobleaching of the $MAPbI_3$ film and mitigates decomposition. In conjunction with these $MAPbI_3$ film studies, we also see a lack of photobleaching in devices with MoO_x interlayers. However, the device stability studies indicate that the presence of a MoO_x interlayer alone is not responsible for alterations to device stability; instead, the specific MoO_x/metal combination plays a critical role. These results suggest that in addition to design rules for maximizing initial efficiency such as tailoring the work function for optimal charge extraction, the evolution of these interfaces may provide a key to understanding the long-term performance of perovskite solar cells. While this work focused on the effects of the back contact on stability for the most commonly used perovskite absorber composition, it is a template and baseline for addressing stability in perovskite solar cells employing alternate absorber compositions or front contacts.

EXPERIMENTAL METHODS

Experimental details are provided in the Supporting Information.

DOI: 10.1021/acsenergylett.6b00013
ACS Energy Lett. 2016, 1, 38–45

■ ASSOCIATED CONTENT

Supporting Information

The Supporting Information is available free of charge on the ACS Publications website at DOI: 10.1021/acsenergylett.6b00013.

Experimental details, additional absorptance spectra, XRD patterns, current density−voltage characteristics in forward and reverse directions for a representative device with a MoO_x/Al electrode, additional XPS data of MoO_x/metal layers, and other additional experimental data (PDF)

■ AUTHOR INFORMATION

Corresponding Author

*E-mail: joey.luther@nrel.gov.

Notes

The authors declare no competing financial interest.

■ ACKNOWLEDGMENTS

Support on this work for B.J.T.d.V., P.S., M.O.R., S.F., K.Z., J.J.B., and J.M.L. was provided by the hybrid perovskite solar cell program of the National Center for Photovoltaics funded by the U.S. Department of Energy, Office of Energy Efficiency and Renewable Energy, Office of Solar Energy Technology under Award Number DE-AC36-08GO28308DOE with the National Renewable Energy Laboratory (NREL). Support for E.M.S. and L.Y.L was provided by the NASA Space Technology Research Fellowship. We thank Bobby To for SEM images, Alfred Hicks for the schematic image, Nathan Neale for TiO_2 nanoparticles, and Arrelaine Dameron for insightful discussions.

■ REFERENCES

(1) *NREL Best Research-Cell Photovoltaic Efficiency Chart*. https://upload.wikimedia.org/wikipedia/commons/archive/3/35/20160317201049%21Best_Research-Cell_Efficiencies.png (accessed Apr 13, 2016).

(2) Jung, H. S.; Park, N.-G. Perovskite Solar Cells: From Materials to Devices. *Small* **2015**, *11*, 10−25.

(3) De Wolf, S.; Holovsky, J.; Moon, S.-J.; Löper, P.; Niesen, B.; Ledinsky, M.; Haug, F.-J.; Yum, J.-H.; Ballif, C. Organometallic Halide Perovskites: Sharp Optical Absorption Edge and Its Relation to Photovoltaic Performance. *J. Phys. Chem. Lett.* **2014**, *5*, 1035−1039.

(4) Ponseca, C. S.; Savenije, T. J.; Abdellah, M.; Zheng, K.; Yartsev, A.; Pascher, T.; Harlang, T.; Chabera, P.; Pullerits, T.; Stepanov, A.; et al. Organometal Halide Perovskite Solar Cell Materials Rationalized: Ultrafast Charge Generation, High and Microsecond-Long Balanced Mobilities, and Slow Recombination. *J. Am. Chem. Soc.* **2014**, *136*, 5189−5192.

(5) Yin, W.-J.; Shi, T.; Yan, Y. Unusual Defect Physics in CH3NH3PbI3 Perovskite Solar Cell Absorber. *Appl. Phys. Lett.* **2014**, *104*, 063903.

(6) Kim, J.; Lee, S.-H.; Lee, J. H.; Hong, K.-H. The Role of Intrinsic Defects in Methylammonium Lead Iodide Perovskite. *J. Phys. Chem. Lett.* **2014**, *5*, 1312−1317.

(7) Burschka, J.; Pellet, N.; Moon, S.-J.; Humphry-Baker, R.; Gao, P.; Nazeeruddin, M. K.; Grätzel, M.; Gratzel, M. Sequential Deposition as a Route to High-Performance Perovskite-Sensitized Solar Cells. *Nature* **2013**, *499*, 316−319.

(8) Zhang, W.; Saliba, M.; Moore, D. T.; Pathak, S. K.; Hörantner, M. T.; Stergiopoulos, T.; Stranks, S. D.; Eperon, G. E.; Alexander-Webber, J. A.; Abate, A.; et al. Ultrasmooth Organic−inorganic Perovskite Thin-Film Formation and Crystallization for Efficient Planar Heterojunction Solar Cells. *Nat. Commun.* **2015**, *6*, 6142.

(9) Ahn, N.; Son, D.-Y.; Jang, I.-H.; Kang, S. M.; Choi, M.; Park, N.-G. Highly Reproducible Perovskite Solar Cells with Average Efficiency of 18.3% and Best Efficiency of 19.7% Fabricated via Lewis Base Adduct of Lead(II) Iodide. *J. Am. Chem. Soc.* **2015**, *137*, 8696−8699.

(10) Yang, W. S.; Noh, J. H.; Jeon, N. J.; Kim, Y. C.; Ryu, S.; Seo, J.; Seok, S., Il. High-Performance Photovoltaic Perovskite Layers Fabricated through Intramolecular Exchange. *Science* **2015**, *348*, 1234−1237.

(11) Abate, A.; Saliba, M.; Hollman, D. J.; Stranks, S. D.; Wojciechowski, K.; Avolio, R.; Grancini, G.; Petrozza, A.; Snaith, H. J. Supramolecular Halogen Bond Passivation of Organic-Inorganic Halide Perovskite Solar Cells. *Nano Lett.* **2014**, *14*, 3247−3254.

(12) Shao, Y.; Xiao, Z.; Bi, C.; Yuan, Y.; Huang, J. Origin and Elimination of Photocurrent Hysteresis by Fullerene Passivation in CH3NH3PbI3 Planar Heterojunction Solar Cells. *Nat. Commun.* **2014**, *5*, 5784.

(13) Noel, N. K.; Abate, A.; Stranks, S. D.; Parrott, E. S.; Burlakov, V. M.; Goriely, A.; Snaith, H. J. Enhanced Photoluminescence and Solar Cell Performance via Lewis Base Passivation of Organic−Inorganic Lead Halide Perovskites. *ACS Nano* **2014**, *8*, 9815−9821.

(14) Lee, M. M.; Teuscher, J.; Miyasaka, T.; Murakami, T. N.; Snaith, H. J. Efficient Hybrid Solar Cells Based on Meso-Superstructured Organometal Halide Perovskites. *Science* **2012**, *338*, 643−647.

(15) Zhou, H.; Chen, Q.; Li, G.; Luo, S.; Song, T. -b.; Duan, H.-S.; Hong, Z.; You, J.; Liu, Y.; Yang, Y. Interface Engineering of Highly Efficient Perovskite Solar Cells. *Science* **2014**, *345*, 542−546.

(16) Niu, G.; Guo, X.; Wang, L. Review of Recent Progress in Chemical Stability of Perovskite Solar Cells. *J. Mater. Chem. A* **2015**, *3*, 8970−8980.

(17) Rong, Y.; Liu, L.; Mei, A.; Li, X.; Han, H. Beyond Efficiency: The Challenge of Stability in Mesoscopic Perovskite Solar Cells. *Adv. Energy Mater.* **2015**, *5*, 1501066.

(18) Niu, G.; Li, W.; Meng, F.; Wang, L.; Dong, H.; Qiu, Y. Study on the Stability of CH 3 NH 3 PbI 3 Films and the Effect of Post-Modification by Aluminum Oxide in All-Solid-State Hybrid Solar Cells. *J. Mater. Chem. A* **2014**, *2*, 705−710.

(19) Yang, J.; Siempelkamp, B. D.; Liu, D.; Kelly, T. L. Investigation of CH3NH3PbI3 Degradation Rates and Mechanisms in Controlled Humidity Environments Using in Situ Techniques. *ACS Nano* **2015**, *9*, 1955−1963.

(20) Conings, B.; Drijkoningen, J.; Gauquelin, N.; Babayigit, A.; D'Haen, J.; D'Olieslaeger, L.; Ethirajan, A.; Verbeeck, J.; Manca, J.; Mosconi, E.; et al. Intrinsic Thermal Instability of Methylammonium Lead Trihalide Perovskite. *Adv. Energy Mater.* **2015**, *5*, 1500477.

(21) Misra, R. K.; Aharon, S.; Li, B.; Mogilyanski, D.; Visoly-fisher, I.; Mogilyansky, D.; Visoly-fisher, I.; Etgar, L.; Katz, E. a. Temperature- and Component-Dependent Degradation of Perovskite Photovoltaic Materials under Concentrated Sunlight. *J. Phys. Chem. Lett.* **2015**, *6*, 326−330.

(22) Kim, J. H.; Williams, S. T.; Cho, N.; Chueh, C.-C.; Jen, A. K.-Y. Enhanced Environmental Stability of Planar Heterojunction Perovskite Solar Cells Based on Blade-Coating. *Adv. Energy Mater.* **2015**, *5*, 1401229.

(23) Christians, J. A.; Miranda Herrera, P. A.; Kamat, P. V.; Herrera, P. A. M.; Kamat, P. V. Transformation of the Excited State and Photovoltaic Efficiency of $CH_3NH_3PbI_3$ Perovskite upon Controlled Exposure to Humidified Air. *J. Am. Chem. Soc.* **2015**, *137*, 1530−1538.

(24) Aristidou, N.; Sanchez-Molina, I.; Chotchuangchutchaval, T.; Brown, M.; Martinez, L.; Rath, T.; Haque, S. A. The Role of Oxygen in the Degradation of Methylammonium Lead Trihalide Perovskite Photoactive Layers. *Angew. Chem., Int. Ed.* **2015**, *54*, 8208−8212.

(25) Wang, D.; Wright, M.; Elumalai, N. K.; Uddin, A. Stability of Perovskite Solar Cells. *Sol. Energy Mater. Sol. Cells* **2016**, *147*, 255−275.

(26) Leijtens, T.; Eperon, G. E.; Noel, N. K.; Habisreutinger, S. N.; Petrozza, A.; Snaith, H. J. Stability of Metal Halide Perovskite Solar Cells. *Adv. Energy Mater.* **2015**, *5*, 1500963.

(27) Reese, M. O.; Gevorgyan, S. A.; Jørgensen, M.; Bundgaard, E.; Kurtz, S. R.; Ginley, D. S.; Olson, D. C.; Lloyd, M. T.; Morvillo, P.;

Katz, E. A.; et al. Consensus Stability Testing Protocols for Organic Photovoltaic Materials and Devices. *Sol. Energy Mater. Sol. Cells* **2011**, *95*, 1253−1267.
(28) Leijtens, T.; Eperon, G. E.; Pathak, S.; Abate, A.; Lee, M. M.; Snaith, H. J. Overcoming Ultraviolet Light Instability of Sensitized TiO2 with Meso-Superstructured Organometal Tri-Halide Perovskite Solar Cells. *Nat. Commun.* **2013**, *4*, 2885.
(29) Kempe, M. D.; Dameron, A. A.; Reese, M. O. Evaluation of Moisture Ingress from the Perimeter of Photovoltaic Modules. *Prog. Photovoltaics* **2014**, *22*, 1159−1171.
(30) Noh, J. H.; Im, S. H.; Heo, J. H.; Mandal, T. N.; Seok, S., Il. Chemical Management for Colorful, Efficient, and Stable Inorganic−Organic Hybrid Nanostructured Solar Cells. *Nano Lett.* **2013**, *13*, 1764−1769.
(31) Lee, J.-W.; Kim, D.-H.; Kim, H.-S.; Seo, S.-W.; Cho, S. M.; Park, N.-G. Formamidinium and Cesium Hybridization for Photo- and Moisture-Stable Perovskite Solar Cell. *Adv. Energy Mater.* **2015**, *5*, 1501310.
(32) Li, X.; DarM, I.; Yi, C.; Luo, J.; Tschumi, M.; Zakeeruddin, S. M.; Nazeeruddin, M. K.; Han, H.; Grätzel, M. Improved Performance and Stability of Perovskite Solar Cells by Crystal Crosslinking with Alkylphosphonic Acid ω-Ammonium Chlorides. *Nat. Chem.* **2015**, *7*, 703−711.
(33) Guarnera, S.; Abate, A.; Zhang, W.; Foster, J. M.; Richardson, G.; Petrozza, A.; Snaith, H. J. Improving the Long-Term Stability of Perovskite Solar Cells with a Porous Al2O3 Buffer-Layer. *J. Phys. Chem. Lett.* **2015**, *6*, 432−437.
(34) Dong, X.; Fang, X.; Lv, M.; Lin, B.; Zhang, S.; Ding, J.; Yuan, N. Improvement of the Humidity Stability of Organic-Inorganic Perovskite Solar Cells Using Ultrathin Al2O3 Layers Prepared by Atomic Layer Deposition. *J. Mater. Chem. A* **2015**, *3*, 5360−5367.
(35) Zheng, L.; Chung, Y.-H.; Ma, Y.; Zhang, L.; Xiao, L.; Chen, Z.; Wang, S.; Qu, B.; Gong, Q. A Hydrophobic Hole Transporting Oligothiophene for Planar Perovskite Solar Cells with Improved Stability. *Chem. Commun.* **2014**, *50*, 11196−11199.
(36) Habisreutinger, S. N.; Leijtens, T.; Eperon, G. E.; Stranks, S. D.; Nicholas, R. J.; Snaith, H. J. Carbon Nanotube/Polymer Composites as a Highly Stable Hole Collection Layer in Perovskite Solar Cells. *Nano Lett.* **2014**, *14*, 5561−5568.
(37) Ono, L. K.; Raga, S. R.; Remeika, M.; Winchester, A. J.; Gabe, A.; Qi, Y. Pinhole-Free Hole Transport Layers Significantly Improve the Stability of MAPbI 3 -Based Perovskite Solar Cells under Operating Conditions. *J. Mater. Chem. A* **2015**, *3*, 15451−15456.
(38) Mei, A.; Li, X.; Liu, L.; Ku, Z.; Liu, T.; Rong, Y.; Xu, M.; Hu, M.; Chen, J.; Yang, Y.; et al. A Hole-Conductor-Free, Fully Printable Mesoscopic Perovskite Solar Cell with High Stability. *Science* **2014**, *345*, 295−298.
(39) Han, Y.; Meyer, S.; Dkhissi, Y.; Weber, K.; Pringle, J. M.; Bach, U.; Spiccia, L.; Cheng, Y.-B. Degradation Observations of Encapsulated Planar CH3NH3PbI3 Perovskite Solar Cells at High Temperatures and Humidity. *J. Mater. Chem. A* **2015**, *3*, 8139−8147.
(40) You, J.; Meng, L.; Song, T.-B.; Guo, T.-F.; Yang, Y.; Chang, W.-H.; Hong, Z.; Chen, H.; Zhou, H.; Chen, Q.; et al. Improved Air Stability of Perovskite Solar Cells via Solution-Processed Metal Oxide Transport Layers. *Nat. Nanotechnol.* **2015**, *11*, 75−81.
(41) Kato, Y.; Ono, L. K.; Lee, M. V.; Wang, S.; Raga, S. R.; Qi, Y. Silver Iodide Formation in Methyl Ammonium Lead Iodide Perovskite Solar Cells with Silver Top Electrodes. *Adv. Mater. Interfaces* **2015**, *2*, 1500195.
(42) Back, H.; Kim, G.; Kim, J.; Kong, J.; Kim, T. K.; Kang, H.; Kim, H.; Lee, J.; Lee, S.; Lee, K. Achieving Long-Term Stable Perovskite Solar Cells via Ion Neutralization. *Energy Environ. Sci.* **2016**, *9*, 1258−1263.
(43) Guerrero, A.; You, J.; Aranda, C.; Kang, Y. S.; Garcia-Belmonte, G.; Zhou, H.; Bisquert, J.; Yang, Y. Interfacial Degradation of Planar Lead Halide Perovskite Solar Cells. *ACS Nano* **2016**, *10*, 218−224.
(44) Zhao, Y.; Nardes, A. M.; Zhu, K. Effective Hole Extraction Using MoOx-Al Contact in Perovskite CH3NH3PbI3 Solar Cells. *Appl. Phys. Lett.* **2014**, *104*, 213906.
(45) Meyer, J.; Hamwi, S.; Kröger, M.; Kowalsky, W.; Riedl, T.; Kahn, A. Transition Metal Oxides for Organic Electronics: Energetics, Device Physics and Applications. *Adv. Mater.* **2012**, *24*, 5408−5427.
(46) Liang, L.; Huang, Z.; Cai, L.; Chen, W.; Wang, B.; Chen, K.; Bai, H.; Tian, Q.; Fan, B. Magnetron Sputtered Zinc Oxide Nanorods as Thickness-Insensitive Cathode Interlayer for Perovskite Planar-Heterojunction Solar Cells. *ACS Appl. Mater. Interfaces* **2014**, *6*, 20585−20589.
(47) Della Gaspera, E.; Peng, Y.; Hou, Q.; Spiccia, L.; Bach, U.; Jasieniak, J. J.; Cheng, Y.-B. Ultra-Thin High Efficiency Semi-transparent Perovskite Solar Cells. *Nano Energy* **2015**, *13*, 249−257.
(48) Matsushima, T.; Kinoshita, Y.; Murata, H. Formation of Ohmic Hole Injection by Inserting an Ultrathin Layer of Molybdenum Trioxide between Indium Tin Oxide and Organic Hole-Transporting Layers. *Appl. Phys. Lett.* **2007**, *91*, 253504.
(49) You, H.; Dai, Y.; Zhang, Z.; Ma, D. Improved Performances of Organic Light-Emitting Diodes with Metal Oxide as Anode Buffer. *J. Appl. Phys.* **2007**, *101*, 026105.
(50) Shrotriya, V.; Li, G.; Yao, Y.; Chu, C.-W.; Yang, Y. Transition Metal Oxides as the Buffer Layer for Polymer Photovoltaic Cells. *Appl. Phys. Lett.* **2006**, *88*, 073508.
(51) Dasgupta, B.; Goh, W. P.; Ooi, Z. E.; Wong, L. M.; Jiang, C. Y.; Ren, Y.; Tok, E. S.; Pan, J.; Zhang, J.; Chiam, S. Y. Enhanced Extraction Rates through Gap States of Molybdenum Oxide Anode Buffer. *J. Phys. Chem. C* **2013**, *117*, 9206−9211.
(52) Pan, H.; Zuo, L.; Fu, W.; Fan, C.; Andreasen, B.; Jiang, X.; Norrman, K.; Krebs, F. C.; Chen, H. MoO3−Au Composite Interfacial Layer for High Efficiency and Air-Stable Organic Solar Cells. *Org. Electron.* **2013**, *14*, 797−803.
(53) Gao, J.; Perkins, C. L.; Luther, J. M.; Hanna, M. C.; Chen, H.-Y.; Semonin, O. E.; Nozik, A. J.; Ellingson, R. J.; Beard, M. C. N-Type Transition Metal Oxide as a Hole Extraction Layer in PbS Quantum Dot Solar Cells. *Nano Lett.* **2011**, *11*, 3263−3266.
(54) Brown, P. R.; Lunt, R. R.; Zhao, N.; Osedach, T. P.; Wanger, D. D.; Chang, L.-Y.; Bawendi, M. G.; Bulović, V. Improved Current Extraction from ZnO/PbS Quantum Dot Heterojunction Photovoltaics Using a MoO3 Interfacial Layer. *Nano Lett.* **2011**, *11*, 2955−2961.
(55) Vasilopoulou, M.; Douvas, A. M.; Georgiadou, D. G.; Palilis, L. C.; Kennou, S.; Sygellou, L.; Soultati, A.; Kostis, I.; Papadimitropoulos, G.; Davazoglou, D.; et al. The Influence of Hydrogenation and Oxygen Vacancies on Molybdenum Oxides Work Function and Gap States for Application in Organic Optoelectronics. *J. Am. Chem. Soc.* **2012**, *134*, 16178−16187.
(56) Bhosle, V.; Tiwari, A.; Narayan, J. Epitaxial Growth and Properties of MoO_x ($2 < x < 2.75$) Films. *J. Appl. Phys.* **2005**, *97*, 083539.
(57) Jasieniak, J. J.; Seifter, J.; Jo, J.; Mates, T.; Heeger, A. J. A Solution-Processed MoOx Anode Interlayer for Use within Organic Photovoltaic Devices. *Adv. Funct. Mater.* **2012**, *22*, 2594−2605.
(58) Chase, M. *J. Phys. Chem. Ref. Data, Monogr. 9* **1998**, 1952.

DOI: 10.1021/acsenergylett.6b00013
ACS Energy Lett. 2016, 1, 38−45